



<b>Publication Year</b>	2017
<b>Acceptance in OA @INAF</b>	2020-08-31T16:24:46Z
<b>Title</b>	Behind the dust curtain: the spectacular case of GRB 160623A
<b>Authors</b>	Pintore, Fabio; Tiengo, A.; MEREGHETTI, Sandro; Vianello, G.; SALVATERRA, Ruben; et al.
<b>DOI</b>	10.1093/mnras/stx2062
<b>Handle</b>	<a href="http://hdl.handle.net/20.500.12386/27006">http://hdl.handle.net/20.500.12386/27006</a>
<b>Journal</b>	MONTHLY NOTICES OF THE ROYAL ASTRONOMICAL SOCIETY
<b>Number</b>	472

# Behind the dust curtain: the spectacular case of GRB 160623A

F. Pintore,<sup>1★</sup> A. Tiengo,<sup>1,2,3</sup> S. Mereghetti,<sup>1</sup> G. Vianello,<sup>4</sup> R. Salvaterra,<sup>1</sup> P. Esposito,<sup>5</sup>  
E. Costantini,<sup>6</sup> A. Giuliani<sup>1</sup> and Z. Bosnjak<sup>7</sup>

<sup>1</sup>INAF – IASF Milano, Via E. Bassini 15, I-20133 Milano, Italy

<sup>2</sup>Scuola Universitaria Superiore IUSS Pavia, Piazza della Vittoria 15, I-27100 Pavia, Italy

<sup>3</sup>Istituto Nazionale di Fisica Nucleare, Sezione di Pavia, Via A. Bassi 6, I-27100 Pavia, Italy

<sup>4</sup>SLAC National Accelerator Laboratory, Stanford University, Stanford, CA 94305, USA

<sup>5</sup>Anton Pannekoek Institute for Astronomy, University of Amsterdam, Postbus 94249, NL-1090-GE Amsterdam, the Netherlands

<sup>6</sup>SRON Netherlands Institute for Space Research, Sorbonnelaan, 2, NL-3584-CA, Utrecht, the Netherlands

<sup>7</sup>Faculty of Electrical Engineering and Computing, University of Zagreb, 10000 Zagreb, Croatia

Accepted 2017 August 8. Received 2017 August 8; in original form 2017 June 22

## ABSTRACT

We report on the X-ray dust-scattering features observed around the afterglow of the gamma-ray burst GRB 160623A. With an *XMM-Newton* observation carried out  $\sim 2$  d after the burst, we found evidence of at least six rings, with angular size expanding between  $\sim 2$  and 9 arcmin, as expected for X-ray scattering of the prompt gamma-ray burst (GRB) emission by dust clouds in our Galaxy. From the expansion rate of the rings, we measured the distances of the dust layers with extraordinary precision:  $528.1 \pm 1.2$ ,  $679.2 \pm 1.9$ ,  $789.0 \pm 2.8$ ,  $952 \pm 5$ ,  $1539 \pm 20$  and  $5079 \pm 64$  pc. A spectral analysis of the ring spectra, based on an appropriate dust-scattering model (BARE-GR-B) and the estimated burst fluence, allowed us to derive the column density of the individual dust layers, which are in the range  $7 \times 10^{20}$ – $1.5 \times 10^{22}$  cm $^{-2}$ . The farthest dust layer (i.e. the one responsible for the smallest ring) is also the one with the lowest column density and it is possibly very extended, indicating a diffuse dust region. The properties derived for the six dust layers (distance, thickness and optical depth) are generally in good agreement with independent information on the reddening along this line of sight and on the distribution of molecular and atomic gas.

**Key words:** scattering – gamma-ray burst: individual: GRB 160623A – dust, extinction – galaxies: haloes – X-rays: bursts – X-rays: ISM.

## 1 INTRODUCTION

Since the advent of X-ray observatories with good imaging capabilities and high throughput, such as *XMM-Newton*, *Chandra* and *Swift*, an increasing number of dust-scattering haloes around bright X-ray sources has been studied in detail. The physical process responsible for the haloes is the small-angle scattering of soft X-ray photons on dust grains in the interstellar medium. Scattered photons form a diffuse halo around the central bright source in the revealed images and, due to their longer path length (which increases with the scattering angle and depends on the distances of the scattering dust from the X-ray source and the observer), are detected with a time delay with respect to the unscattered photons. Therefore, changes in the intensity and radial profile of the halo can be seen in the case

of variable sources. A particularly simple case is provided by impulsive sources which are very bright only for a short time interval, such as gamma-ray bursts (GRBs), bursts from magnetars and type I X-ray bursts from accreting neutron stars. The halo characteristics are also affected by the distribution of the dust along the line of sight. For narrow dust clouds, the haloes produced by impulsive sources appear as rings.

Haloes and expanding rings have been detected around Galactic binary systems (e.g. Heinz et al. 2015, 2016; Vasilopoulos & Petropoulou 2016), magnetars (e.g. Tiengo et al. 2010; Svirski, Nakar & Ofek 2011; Pintore et al. 2017) and GRBs (e.g. Vaughan et al. 2004; Tiengo & Mereghetti 2006; Vianello, Tiengo & Mereghetti 2007). The study of the energy- and time-dependence of scattering haloes can provide important information on the chemical composition, grain size and spatial distribution of the dust, as well as on the distance of the X-ray sources (e.g. Trümper & Schönfelder 1973; Mathis & Lee 1991; Miralda-Escudé 1999;

★ E-mail: [pintore@iasf-milano.inaf.it](mailto:pintore@iasf-milano.inaf.it)

Predehl et al. 2000; Draine 2003; Costantini, Freyberg & Predehl 2005).

In the case of X-ray photons of a burst source at distance  $d$  scattering on a narrow layer of dust at distance  $d_{\text{dust}}$ , the ring angular radius  $\theta(t)$  can be expressed as

$$\theta(t) = \left[ \frac{2c}{d} \frac{(1-x)}{x} (t - T_0) \right]^{0.5}, \quad (1)$$

where  $x = d_{\text{dust}}/d$ ,  $c$  is the speed of light and  $T_0$  is the time of the burst. When  $d \gg d_{\text{dust}}$ , as for GRBs scattering on dust clouds in our Galaxy, the above expression simplifies to

$$\theta(t) = \left[ \frac{2c(t - T_0)}{d_{\text{dust}}} \right]^{0.5} = K(t - T_0)^{0.5}, \quad (2)$$

where the degeneracy between the source and the dust-layer distances is removed. Therefore, by measuring the rate of the angular expansion of the ring, one can obtain a very accurate, model-independent, measure of the dust-layer distance. The scattering rings may also have an intrinsic width  $\Delta\theta$ , which depends on the thickness of the dust layer and on the duration of the impulse emission. The observed width is also affected by the finite angular resolution of the instrument and by the ring expansion during the integration time needed to detect it.

In this work, we study the bright dust-scattering rings produced by GRB 160623A. This GRB, discovered by the *Fermi*/GBM instrument and detected also above 1 GeV with the *Fermi*/LAT (Vianello et al. 2016), was located at Galactic coordinates  $l = 84^\circ.2$ ,  $b = -2^\circ.7$  which is a direction crossing a long path of our Galaxy, where dust clouds are expected. GRB 160623A was also detected by Konus-Wind, with a start time at  $T_0 = 04:59:37.594$  UT. The 50 keV–15 MeV spectrum of the burst, averaged from  $T_0$  to  $T_0 + 38.912$  s, was well fitted by a *Band* function with  $\alpha = -1.05 \pm 0.03$ ,  $\beta = -2.67 \pm 0.1$ , and peak energy  $E_p = 562 \pm 23$  keV; the fluence in the 20 keV–10 MeV range was  $(6.6 \pm 0.1) \times 10^{-4}$  erg cm $^{-2}$  (Frederiks et al. 2016). The *Swift*/XRT observations of GRB 160623A started  $\sim 40$  ks after  $T_0$ , and showed an X-ray afterglow surrounded by a dust-scattering ring with the radius of  $\sim 3.5$  arcmin (Tiengo et al. 2016). A quick look analysis of the XRT data indicated that the ring was produced by at least one Galactic dust cloud at a distance of  $\sim 800$  pc.

The optical afterglow of GRB 160623A was observed by the Nordic Optical Telescope (NOT) and the Gran Telescopio Canarias (GTC) (Castro-Tirado et al. 2016; Malesani et al. 2016). H $\alpha$ , S II and N II emission lines were detected at a redshift of  $z = 0.367$ , corresponding to a distance of  $\sim 1530$  Mpc.

After finding the evidence of dust scattering rings in the *Swift*/XRT data, we triggered an *XMM-Newton* target of opportunity observation to study the rings in more detail and characterize the properties of the dust clouds in this direction.

## 2 DATA REDUCTION

The *XMM-Newton* observation of GRB 160623A started at 21:04 UT of 2016 June 24,  $\sim 2$  d after the burst, and lasted for about 16 h. We used the data obtained with the pn (Strüder et al. 2001) and the two MOS cameras (Turner et al. 2001) of the EPIC instrument. They were operated in the full-frame mode, providing 0.2–12 keV images over a field of view of  $\sim 27$  arcmin  $\times$  27 arcmin, and with a thin optical blocking filter. We reduced the data with the *SAS* v15.0.0 software, selecting single- and double-pixel events (*PATTERN*  $\leq 4$ ) for

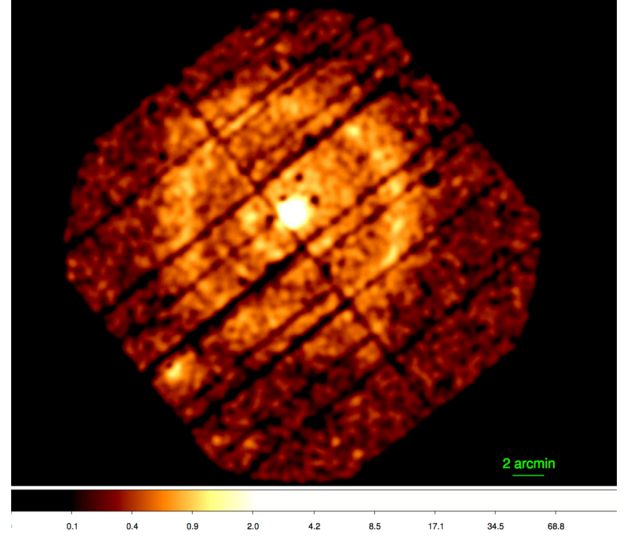


**Figure 1.** EPIC-pn image (colour bar in counts pixel $^{-1}$ ) in the 1–2 keV energy band: dust-scattering rings extending up to 9 arcmin are visible around the GRB afterglow. North is up, and east to the left. The Galactic Centre is towards the west side of the image.

the pn and single- and multiple-pixel events for the MOS (*PATTERN*  $\leq 12$ ). After removing  $\sim 1.5$  ks of data affected by high particle-background events in the initial part of the observation, we obtained net exposure times of  $\sim 50$  ks in the pn and  $\sim 55$  ks in the MOS.

The image obtained with the pn camera in the 1–2 keV energy range is shown in Fig. 1, where a bright afterglow at the GRB position and the prominent dust scattering rings can be clearly seen. To derive the properties of the scattering rings, we removed from the event files all the brightest point-like sources in the field of view and we removed the out-of-time events<sup>1</sup> in the EPIC-pn data.<sup>2</sup>

The spectra and light curves of the afterglow were extracted from a circular region with radius of 35 arcsec centred at the GRB position (R.A. = 315 $^{\circ}$ :298 59, Dec. = 42 $^{\circ}$ :221 236) while the background was extracted from a circular region of radius 60 arcsec on the same CCD and not containing sources and scattered emission.

The spectral fits were carried out with the *XSPEC* v12.8.2 software package (Arnaud 1996), adopting the *TBABS* model for the interstellar absorption with solar abundances of Wilms, Allen & McCray (2000). In the following, all the errors in the spectral parameters are given at the 90 per cent confidence level for a single interesting parameter.

## 3 DATA ANALYSIS AND RESULTS

### 3.1 Afterglow

The light curve of the X-ray afterglow of GRB 160623A is plotted in Fig. 2, where a smooth count rate decrease of about a factor of 2 between the start and the end of the observation can be seen.

<sup>1</sup> When *XMM-Newton*/EPIC is operated in the IMAGING mode, out-of-time events are generated when a photon hits the CCD during the read-out process. This results in the knowledge of the event  $x$  position but not of its  $y$  position because of the readout and shifting of the charges. This effect is much stronger in the pn than in the MOS cameras.

<sup>2</sup> As described in the *XMM-Newton* thread <https://www.cosmos.esa.int/web/xmm-newton/sas-thread-epic-oot> in the case of the Full-Frame mode.

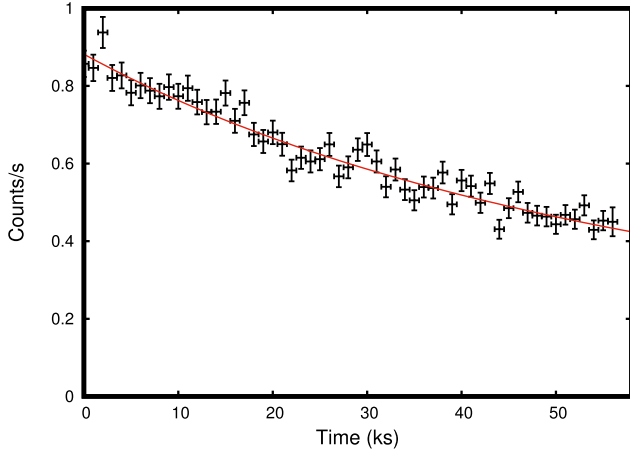


**Figure 2.** EPIC-pn background-subtracted light curve of the GRB afterglow in the energy range 0.3–10 keV sampled with a bin size of 1 ks. The decay is modelled by a power-law function (red solid line) with an index of  $-2.11 \pm 0.07$  ( $\chi^2/\text{dof} = 1.2$ ).

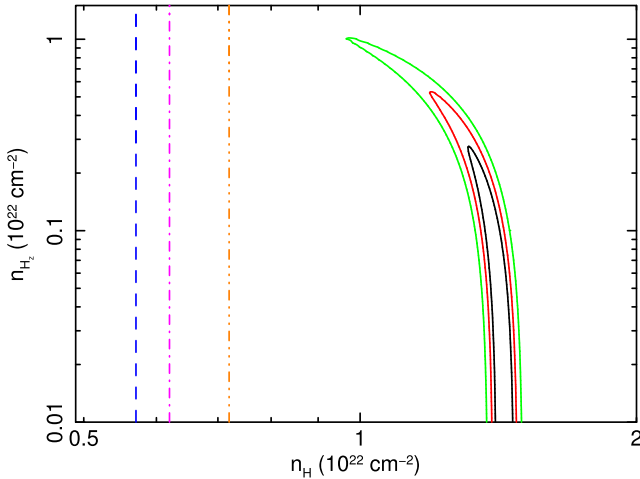


**Figure 3.** Contour plot, at  $1\sigma$  (black),  $2\sigma$  (red) and  $3\sigma$  (green) uncertainties, of the Galactic  $n_{\text{H}}$  and  $n_{\text{H}_z}$ . The plot shows a significant degeneracy for the two parameters. The blue dashed, the fuchsia dot-dashed and the orange double-dot-dashed lines represent the Galactic column density expected along the line of sight ( $6.2 \times 10^{21} \text{ cm}^{-2}$  for Dickey & Lockman 1990,  $5.7 \times 10^{21} \text{ cm}^{-2}$  for Kalberla et al. 2005 and  $7.2 \times 10^{21} \text{ cm}^{-2}$  for Willingale et al. 2013).

The decay can be described by a power law  $F(t) \propto t^\alpha$  with  $\alpha = -2.11 \pm 0.07$ .

The time-averaged spectrum of the afterglow is well described ( $\chi^2/\text{dof} = 971.05/1036$ ) by a power law with photon index  $1.77 \pm 0.03$ , modified by a Galactic plus a host galaxy ( $z = 0.367$ ) absorption. The best-fitting value of the Galactic absorption is  $n_{\text{H}} = (1.44^{+0.04}_{-0.15}) \times 10^{22} \text{ cm}^{-2}$ , while that of the host galaxy,  $n_{\text{H}_z}$ , is poorly constrained and with a best-fitting value significantly lower than  $10^{21} \text{ cm}^{-2}$ , as can be seen in Fig. 3. The absorbed (unabsorbed) 0.3–10 keV flux is  $(3.44 \pm 0.05) \times 10^{-12} \text{ erg cm}^{-2} \text{ s}^{-1}$  ( $(5.9 \pm 0.1) \times 10^{-12} \text{ erg cm}^{-2} \text{ s}^{-1}$ ). The spectral shape and the column density are consistent with those found with *Swift*/XRT (Mingo et al. 2016). We note that the best-fitting Galactic column density is more than a factor of 2 larger than the total column density expected along this line of sight ( $6.2 \times 10^{21} \text{ cm}^{-2}$  for Dickey

& Lockman 1990;  $5.7 \times 10^{21} \text{ cm}^{-2}$  for LAB, Kalberla et al. 2005;  $7.2 \times 10^{21} \text{ cm}^{-2}$  for Willingale et al. 2013).

To investigate this discrepancy better, we analysed an extended source detected by EPIC in the same observation, at coordinates  $\text{RA} = 21^{\text{h}}01^{\text{m}}51^{\text{s}}$ ,  $\text{Dec} = +42^\circ03'24''$ , at an angular distance of  $\sim 12.3$  arcmin from GRB 160623A. The spectral shape and extended nature suggest that this source is a cluster of galaxies. We fitted its spectrum with an absorbed collisionally ionized diffuse gas model (APEC in XSPEC) and found a temperature of  $kT = 4.5^{+2.5}_{-1.2} \text{ keV}$  and a column density of  $(7 \pm 2) \times 10^{21} \text{ cm}^{-2}$ , fully consistent with the  $n_{\text{H}}$  expected from Willingale et al. (2013). With the assumption that the column density in the directions of GRB 160623A and of this source is the same, we fitted the afterglow spectrum with  $n_{\text{H}}$  fixed to  $7.2 \times 10^{21} \text{ cm}^{-2}$ . A good fit ( $\chi^2/\text{dof} = 985.33/1037$ ) was obtained with  $n_{\text{H}_z} = (1.60 \pm 0.08) \times 10^{22} \text{ cm}^{-2}$  and a 0.3–10 keV absorbed (unabsorbed) flux of  $(2.7 \pm 0.4) \times 10^{-12} \text{ erg cm}^{-2} \text{ s}^{-1}$  ( $(4.0 \pm 0.5) \times 10^{-12} \text{ erg cm}^{-2} \text{ s}^{-1}$ ).

### 3.2 Dust rings

To illustrate the angular expansion of the rings, we created four EPIC-pn images in the 1–2 keV energy band, corresponding to consecutive time intervals of  $\sim 14$  ks each (Fig. 4). They clearly show the presence of at least three expanding rings, with average radii of  $\sim 3.2$ ,  $\sim 5.2$  and  $\sim 7.3$  arcmin. The outer ring is broader than the others and shows the most prominent expansion. Describing the angular expansion as  $\theta = K(t - T_0)^{1/2}$ , with  $\theta$  in arcmin and  $(t - T_0)$  in days ( $T_0$  is the GRB time and  $t$  is the mean time of the *XMM-Newton* observation), we estimated  $K \sim 2.3$ ,  $3.7$ , and  $5.2$  arcmin  $\text{d}^{-0.5}$  for the three rings. Using equation (2), these expansion coefficients correspond to dust distances of  $\sim 4$ ,  $\sim 1.5$  and  $\sim 0.7$  kpc, respectively. Therefore, the outermost ring is compatible with being the one detected by *Swift*/XRT at earlier times and for which Tiengo et al. (2016) estimated  $d \sim 0.8$  kpc.

To increase the sensitivity for the detection of faint expanding rings not easily seen in the time integrated images of Fig. 4, we used the method based on so called *dynamical images* first introduced by Tiengo & Mereghetti (2006). A dynamical image is created by converting the detector position ( $x_i$  and  $y_i$ ) and time of arrival ( $T_i$ ) of each event into a new set of coordinates given by

$$t_i = T_i - T_0$$

$$\theta_i^2 = (x_i - X_{\text{GRB}})^2 + (y_i - Y_{\text{GRB}})^2$$

where  $T_0$ ,  $X_{\text{GRB}}$  and  $Y_{\text{GRB}}$  are the GRB start time and spatial coordinates (the latter are derived from the afterglow position in this observation). In an image based on these coordinates, a (non-variable) source appears as a horizontal line at constant  $\theta^2$ , while an expanding ring centred at  $X_{\text{grb}}$ ,  $Y_{\text{grb}}$  appears as an inclined line with an angular coefficient proportional to the distance of the dust-scattering layer.

We first performed this analysis separately on the data of the three EPIC cameras and did not find any significant difference. We then stacked the pn and MOS events to increase the signal-to-noise ratio and hereafter, unless explicitly stated, we shall always refer to the combination of the EPIC data. In Fig. 5, we show the *dynamical image* in the 1–2 keV energy range, where at least six inclined lines associated with the dust-scattering rings are visible. We note that with this method we can identify more rings than in a simple study of the radial profile of the EPIC sky image.



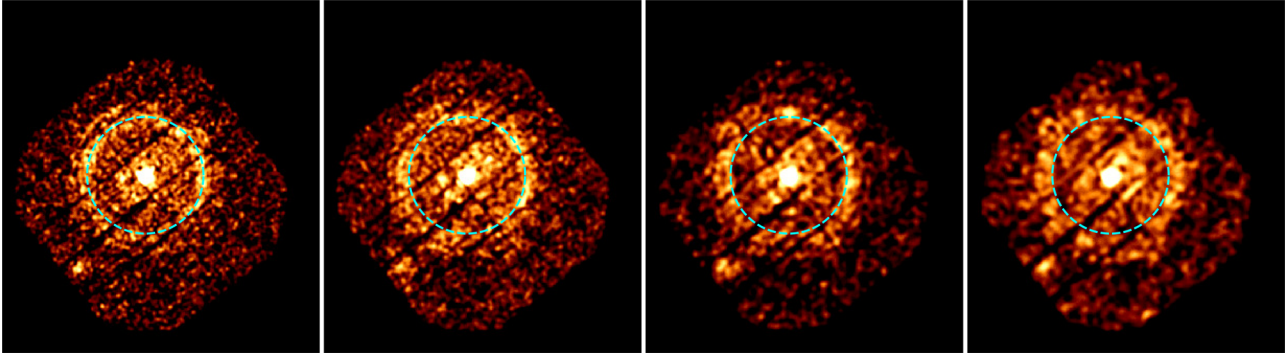


**Figure 4.** EPIC-pn images in the 1–2 keV energy band, integrated for consecutive intervals of 14 ks starting from the beginning of the observation. The cyan dashed circle (radius of 6.4 arcmin) is a reference to show better the outer rings expansion. Time increases from left to right.

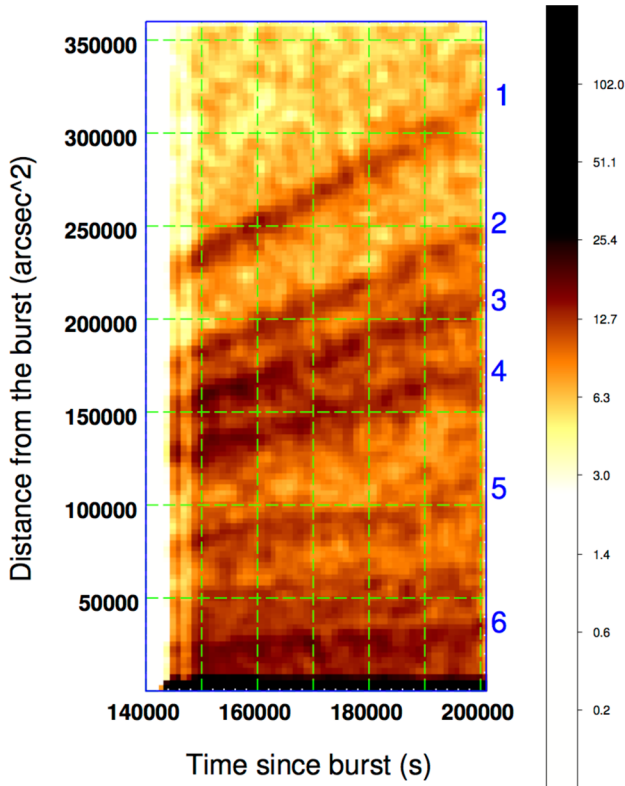


**Figure 5.** Dynamical image (colour bar in counts pixel<sup>−1</sup>) of the EPIC-(pn+MOS) data in the 1–2 keV energy range. The numbers on the right axis label the different rings.

Following Tiengo & Mereghetti (2006) and, for each event, we can define a *pseudo-distance*  $D_i$  as

$$D_i = 2ct_i/\theta_i^2 = 827t_i[s]/\theta_i^2[\text{arcsec}] \text{ pc}.$$

We called it *pseudo-distance* as it assigns a distance to both background and source/expanding ring events. Clearly, for background events, this value is not a real distance. On the other hand, events coming from an expanding ring cluster around a specific value of  $D$  which corresponds to the ‘true’ dust-layer distance. Hence, to derive quantitatively the properties of the rings, we created a histogram of the pseudo-distances (Fig. 6-left), corrected for the exposure time. In this histogram, the background counts form a smoothly decaying continuum while the rings appear as individual peaks. A uniform background should be described by a power law with index  $-2$ . On

the other hand, the background component due to the diffuse X-ray emission is subject to telescope vignetting effects, which produce a significant deviation from the expected power law. Indeed, we found that the continuum shape can be described with the sum of two power laws with indexes of  $-1.91 \pm 0.08$  and  $-2.87 \pm 0.20$ . The peaks due to the rings are instead well described by Lorentzian functions. By fitting the pseudo-distance histograms with these models, we can estimate the statistical significance of the rings seen in the dynamical images: we found that the addition of *each* of the six Lorentzian models significantly improves the reduced  $\chi^2$ , with an F-test probability that the improvement is not obtained by chance  $\gg 5\sigma$  (for three additional degree of freedom). The histogram in the 1–2 keV energy range and the best fit with two power laws and six Lorentzians are shown in Fig. 6(left), while in Fig. 6(right) we show the residuals (in units of  $\sigma$ ) of the fit with only the continuum. The best-fitting centroids of the Lorentzians give accurate measurements of the distances of the dust layers, which range from  $528.1 \pm 1.2$  to  $5079 \pm 64$  pc (see Table 1 for all the values).

We estimated, through simulations using the EPIC point spread function<sup>3</sup> (PSF), that the best-fitting FWHMs of the two innermost rings are slightly larger than the expected instrumental broadening (although consistent within  $2\sigma$  uncertainty) while those of the other rings are instead significantly larger. The corresponding thicknesses of the dust layers are given in Table 1.

Finally, we also note in Fig. 6 the presence of two other, weaker peaks at  $\sim 2.5$  and  $\sim 3$  kpc. We excluded them from the analysis because their properties could be only poorly constrained.

### 3.3 Spectral analysis of the rings

A standard extraction of the spectra of the rings (i.e. selecting the counts from annular regions in the EPIC images) presents some critical issues. In fact, due to their expansion during the observation, the rings spatially overlap. The selection of fixed annular regions would yield spectra with mutual contamination of the adjacent rings. In addition, it would be difficult to select background regions because most of the field of view is covered by the rings. The best approach to overcome these problems is to extract directly the background-subtracted spectra by integrating the Lorentzian functions fitted to the histograms of the pseudo-distances for different energy bins.

<sup>3</sup> We used the analytical model of Ghizzardi (2002, XMM-SOC-CAL-TN-0029), which accurately describes the spatial and energy dependence of the EPIC-PSF, but not its azimuthal structure (see Read et al. 2011).

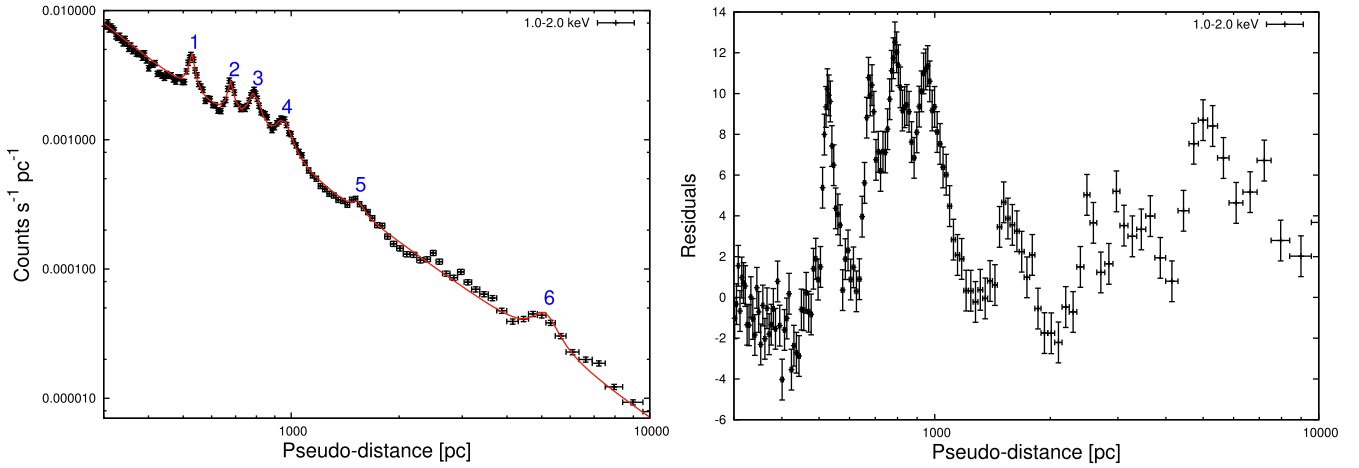


**Figure 6.** Left-hand panel: histogram pseudo-distances of the EPIC-pn+MOS instruments (black points) in the 1.0–2.0 keV energy band, fitted with two power laws plus six Lorentzian functions (red solid line). We grouped the data in order to have at least 500 counts in each bin. The numbers, from 1 to 6, represent the label of the ring. Right-hand panel: residuals (in units of  $\sigma$ ) of the best fit with two power laws with index  $-1.91 \pm 0.08$  and  $-2.87 \pm 0.20$ . In both plots, six strong features are clearly visible at distances of  $\sim 530, 680, 790, 950, 1540$  and  $5080$  pc.

**Table 1.** Column density of the interstellar medium and of the dust layers, and their corresponding unabsorbed fluxes in the 0.3–10 keV energy range, as estimated by the fits of the ring spectra. Errors at 90 per cent confidence level.

	$n_{\text{H,dust}}$ ( $10^{21} \text{ cm}^{-2}$ )	Flux ( $\text{erg cm}^{-2} \text{ s}^{-1}$ )	Distance (pc)	Width (pc)
Ring 1	$6.9^{+0.7}_{-0.6}$	$1.1 \times 10^{-12}$	$528.1 \pm 1.2$	$23.4 \pm 3.3$
Ring 2	$4.5^{+0.5}_{-0.4}$	$0.66 \times 10^{-12}$	$679.2 \pm 1.9$	$32.3 \pm 5.7$
Ring 3	$14.6^{+1.2}_{-1.1}$	$2.1 \times 10^{-12}$	$789.0 \pm 2.8$	$75 \pm 10$
Ring 4	$5.0^{+0.4}_{-0.4}$	$0.66 \times 10^{-12}$	$952 \pm 5$	$116 \pm 15$
Ring 5	$11.4^{+2.1}_{-2.1}$	$1.2 \times 10^{-12}$	$1539 \pm 20$	$106 \pm 60$
Ring 6	$0.7^{+0.1}_{-0.1}$	$0.045 \times 10^{-12}$	$5079 \pm 64$	$1000 \pm 400$

The rings are spectrally soft and detected with the highest significance in the 0.5–2.5 keV range. We divided this range in different bins and for each one we created the histogram of the pseudo-distances. We fixed the slopes of the continuum power laws, as well as the centroids and widths of the Lorentzians, to their values obtained in the total 0.5–2.5 keV histogram; we then fitted only the normalizations of the power laws and of the Lorentzians in each energy bin. By integrating the best-fitting Lorentzian functions, we obtained the background-subtracted ring spectra shown in Fig. 7. They clearly show that rings from 1 to 5 have similar fluxes (rings 3 and 5 are the brightest), while ring 6 is significantly fainter but its spectrum is the hardest one.

The intensity of each ring as a function of time and energy depends on the spectrum and fluence of the burst and on the optical depth of the corresponding dust layer. To derive the latter quantity from a fit of the ring spectra, we followed the procedure outlined in Shao & Dai (2007). We adopted the grain composition and size distribution of the *BARE-GR-B* model<sup>4</sup> presented in Zubko et al. (2004), which was found to describe quite well the properties of dust layers in the Galaxy (see e.g. Tiengo et al. 2010; Jin et al. 2017;

<sup>4</sup>This model includes polycyclic aromatic hydrocarbons (PAH), silicate grains and bare graphite grains with the abundances of B-type stars. See fig. 14 of Zubko, Dwek & Arendt (2004) for a comparison with the dust-distribution from Mathis, Rumpl & Nordsieck (1977).

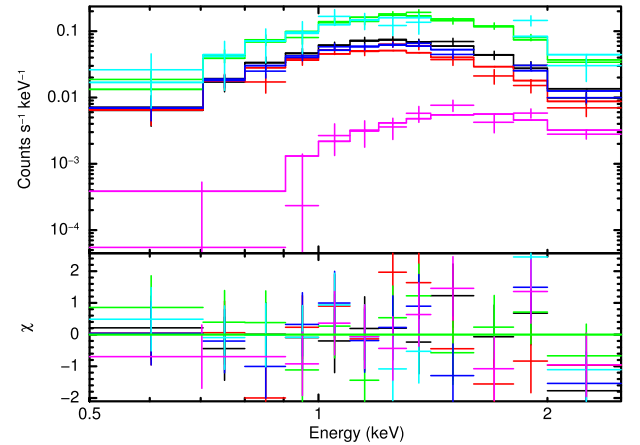


**Figure 7.** Spectra of the dust-scattering rings (top-panel) fitted with a  $\text{TBABS} \times \text{CONSTANT} \times \text{DUST-MODEL}$  model and the corresponding residuals (bottom panel). The black, red, green, blue, cyan and purple points represent data from ring 1, ring 2, ring 3, ring 4, ring 5 and ring 6, respectively. Because of a strong background contamination, some spectral points were removed around the energy of the instrumental Al feature ( $\sim 1.5$  keV) for rings 4 and 5.

Pintore et al. 2017). To compute the expected spectrum of each ring at the time of the *XMM-Newton* observation, we used the Rayleigh–Gans approximation for the scattering cross-section, the dust distances derived above and the burst fluence obtained by extrapolating the Konus–Wind spectrum ( $1.2 \times 10^{-5} \text{ erg cm}^{-2}$  in the 0.3–10 keV range). The resulting model, which we implemented as a *TABLE MODEL* in *XSPEC*, has as free parameter only the normalization, which gives the dust column density  $n_{\text{H,dust}}$  of the scattering layer. For each spectrum, we created response matrices and ancillary files (for extended sources) for an annular region with inner and outer radii defined by the region swept by the ring centroids from the start to the stop time of the observation. The arf files were created by taking into account the exposure map also in the selected annular regions. In the range 1.3–1.6 keV, the background continuum was significantly affected by the instrumental Al feature (at 1.49 keV) and such a contamination was particularly prominent for rings 4

and 5. Due to the resulting poor characterization of the continuum, we excluded this energy bin from the spectra of rings 4 and 5.

We fitted simultaneously the ring spectra including Galactic absorption with  $n_{\text{H}}$  linked to a common value (TBABS×DUST in XSPEC). We found a good fit ( $\chi^2/\text{dof} = 67.46/54$ ) with  $n_{\text{H}} = (1.04 \pm 0.06) \times 10^{22} \text{ cm}^{-2}$  and the dust-column density values for the dust layers shown in Table 1. They are in the range  $\sim 0.07\text{--}1.5 \times 10^{22} \text{ cm}^{-2}$  and give a total dust column density of  $\sim 4.3 \times 10^{22} \text{ cm}^{-2}$ . This is larger than the value of the Galactic column density expected along the line of sight ( $7.2 \times 10^{21} \text{ cm}^{-2}$ ; Willingale et al. 2013) and the value ( $1.44 \times 10^{22} \text{ cm}^{-2}$ ) derived from our fit to the afterglow spectrum with Galactic and host absorption as free parameters. Such a discrepancy may be explained considering that values of the dust grain-to-hydrogen atom ratio larger than 1 have been observed also in other Galactic clouds (see e.g. Vuong et al. 2003; Hasenberger et al. 2016; Pintore et al. 2017). The difference is likely due to the fact that the gas-to-dust ratio is not homogenous in the Galaxy, while the normalization of the dust model we adopted here is based on an average value of this ratio. Alternatively, one is forced to conclude that the soft X-ray burst fluence we derived by extrapolating the Konus-Wind spectrum is actually underestimated by at least a factor of  $\sim 6(3)$  to be in accordance with the column density of  $7.2 \times 10^{21} \text{ cm}^{-2}$  ( $1.44 \times 10^{22} \text{ cm}^{-2}$ ).

Finally we note that the adopted Rayleigh–Gans approximation, used to calculate the scattering cross-section, assumes that photon wavelengths are much larger than the grain size, the shape of the grain is spherical, the photon absorption is negligible and the scattering angle is small (e.g. Smith & Dwek 1998). For the expected sizes of the interstellar dust grains, such assumptions are generally valid for X-ray photons  $\geq 1 \text{ keV}$ . For this reason, we also checked the goodness of such approximation in our analysis and we fitted the spectra for energies  $> 1 \text{ keV}$ , finding that the dust-column densities are fully consistent with those inferred in the broader energy range. This implies that, although the Rayleigh–Gans approximation may not be fully satisfied, it does not significantly affect our results.

#### 4 DISCUSSION

The good imaging capabilities and high sensitivity of the *XMM-Newton*/EPIC detectors, and the use of an ad hoc analysis technique based on ‘dynamical-images’, allowed us to find evidence of at least six expanding rings around the position of GRB 160623A.

The expansion rate of the rings allowed us to derive a dynamical measure of the dust-layer distances (see Table 1). Remarkably, the distances of the dust layers are constrained with a precision of less than 1 per cent just basing the analysis on simple geometrical considerations, which makes this the best characterization by far of the Galactic clouds along this line of sight. The *Swift*/XRT data, taken 40 ks after the GRB revealed a halo produced by dust at a distance of  $\sim 800 \text{ pc}$  (Tiengo et al. 2016), which we can associate with ring 3, i.e. the one with the highest column density.

Knowing the dust distances, with the assumed GRB X-ray fluence and the derived column densities, we can compute the light curves of the six rings and compare them with that of the burst afterglow. This is shown in Fig. 8, where we plot the light curves of the single rings and of their sum for the time interval from 1000 s to  $10^6$  s after the GRB. The afterglow light curve in the 0.3–10 keV range, based on the *XMM-Newton* and *Swift*/XRT data<sup>5</sup>, is well described

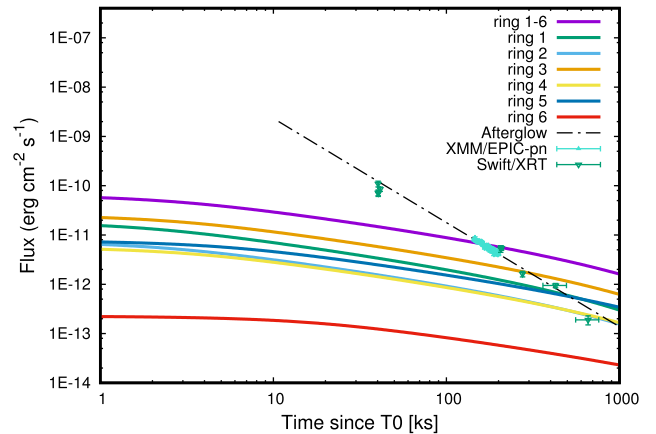


**Figure 8.** Unabsorbed 0.3–10 keV flux of the *XMM-Newton*/EPIC-pn (cyan filled triangles) and *Swift*/XRT observations (green filled reversed triangles) of the GRB 160623A afterglow. The black dashed line shows the flux extrapolated from the best-fitting power law of the *XMM-Newton* EPIC-pn data. The solid lines represent instead the dust-model light curves. The total contribution of the dust-scattering flux decays less quickly than the afterglow and dominates the emission starting  $\sim 100$  ks after the GRB.

by a power-law decay. Initially, the afterglow is much brighter than the rings, but after  $\sim 100$  ks the total emission of the rings becomes dominant. This clearly indicates that the dust-scattered radiation can be significantly detected even when the GRB afterglow has faded at lower fluxes. However, we note that we computed these light curves assuming a homogeneous distribution of the dust in the plane perpendicular to the line of sight. If the dust clouds were not homogenous, the light curves would differ from those shown in Fig. 8. It is also interesting to note that, for small redshifts ( $z < 1$ ), the same light curve would have been obtained if the dust clouds, with these relative distances and column densities, were located in the host galaxy. However, in such a case it would have been impossible to resolve spatially the rings and the whole emission would have been attributed to the afterglow. Indeed, it has been proposed that dust-scattering effects in the GRB host galaxies can, in some cases, be responsible for features seen in the light curves of the afterglows (e.g. Shao & Dai 2007). In fact, there exists a subclass of GRBs, characterized by plateaus in the early phases after the GRB pulse, a softening of their X-ray flux on longer time-scales and long-lasting emission, where dust-scattering processes has been shown to be important (e.g. Evans et al. 2014; Zhao & Shao 2014; Wang et al. 2016).

To compare the properties we derived for the dust in the direction of GRB 160623A with the Galactic distribution of molecular clouds, we used the  $\text{H I}$  and  $\text{H}_2$  surveys of Dame, Hartmann & Thaddeus (2001) and Kalberla et al. (2005) (Fig. 9). The  $\text{H}_2$  profiles show that most of the material is located within less than 3 kpc, with a peak at  $\sim 2 \text{ kpc}$ . On the other hand, the  $\text{H I}$  profile presents a significant peak at  $\sim 0.5\text{--}1 \text{ kpc}$  and also indicates the existence of other material in the range 2–6 kpc. The recent paper of Rice et al. (2016) investigated all the molecular clouds with masses  $> 10^4 M_{\odot}$ , but none were found along the GRB 160623A direction.

The first peak in the  $\text{H I}$  profile can be associated with the four closest clouds identified in our work, which contain most of the dust along the line of sight. The  $\text{H I}$  profile also shows an extended region with lower density from about 2 to 6 kpc, which can be tentatively associated with the dust layer at  $\sim 5.1 \text{ kpc}$  (ring 6). This layer is also the one with the lowest column density ( $\sim 7 \times 10^{20} \text{ cm}^{-2}$ ) and the corresponding ring has the hardest spectrum. It therefore contains

<sup>5</sup> Obtained by the online tool described in Evans et al. (2009). See [http://www.swift.ac.uk/user\\_objects/](http://www.swift.ac.uk/user_objects/)



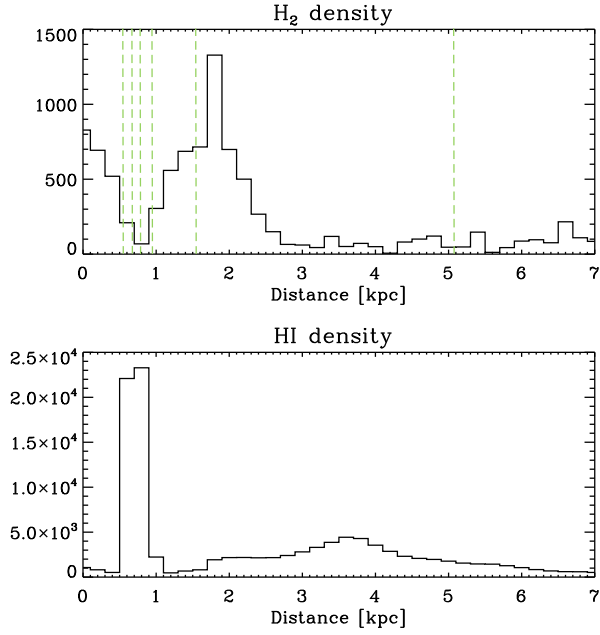


**Figure 9.** Galactic density profiles in unity of  $10^4$  atoms  $\text{cm}^{-3}$  of the  $\text{H I}$  and  $\text{H}_2$  clouds towards the direction of the GRB. In each step of the histogram, the uncertainties on the densities are 20 per cent and 40 per cent for  $\text{H}_2$  and  $\text{H I}$ . The dashed lines indicate the position of the dust layers found in this work.

a small amount of dust grains and we could find evidence of it only because its radial expansion was still small during the *XMM-Newton* observation (which, in turns, implies a large cross-section). In particular, the broad peak in the pseudo-distance distribution indicates that this dust layer may be significantly extended. We can locate this dust inside the Perseus spiral arm of the Galaxy and we speculate that this may be a large region of diffuse dust rather than a single cloud. Although definitely fainter and very poorly constrained, we cannot exclude that the tentative rings detected at  $\sim 2.5$  and  $\sim 3$  kpc also might be associated with the same large Galactic structure. Instead, from the  $\text{H}_2$  profile, the bulk of the density is located closer than 700 pc or between  $\sim 1$  and 3 kpc. The dust layers of rings 1–4 could be associated with the first bunch of material, while the dust layer detected at  $\sim 1.5$  kpc to the second one. In addition, we note that the Galactic micro-quasar V404 Cyg (at RA, Dec = (315°30, 42°22)) is about  $11^\circ$  far from GRB 160623A, and the line of sight towards both sources intersects the Orion Spur. In 2015, after a bright outburst, five expanding rings were observed around V404 Cyg (Beardmore et al. 2016; Heinz et al. 2016) and the corresponding dust layers located at distances of  $\sim 1200$ , 1500, 1600, 2050 and 2100 pc. We can tentatively associate the dust layers at  $\sim 1500$  and 1600 pc found for V404 Cyg with the one responsible for ring 5 in this work, but, considering the elongated structure of the Orion spur and that  $11^\circ$  at distances between 500 and 2000 pc correspond to a separation ranging from  $\sim 100$  to  $\sim 400$  pc, we do not expect a close correspondence between the clouds detected along these relatively distant lines of sight.

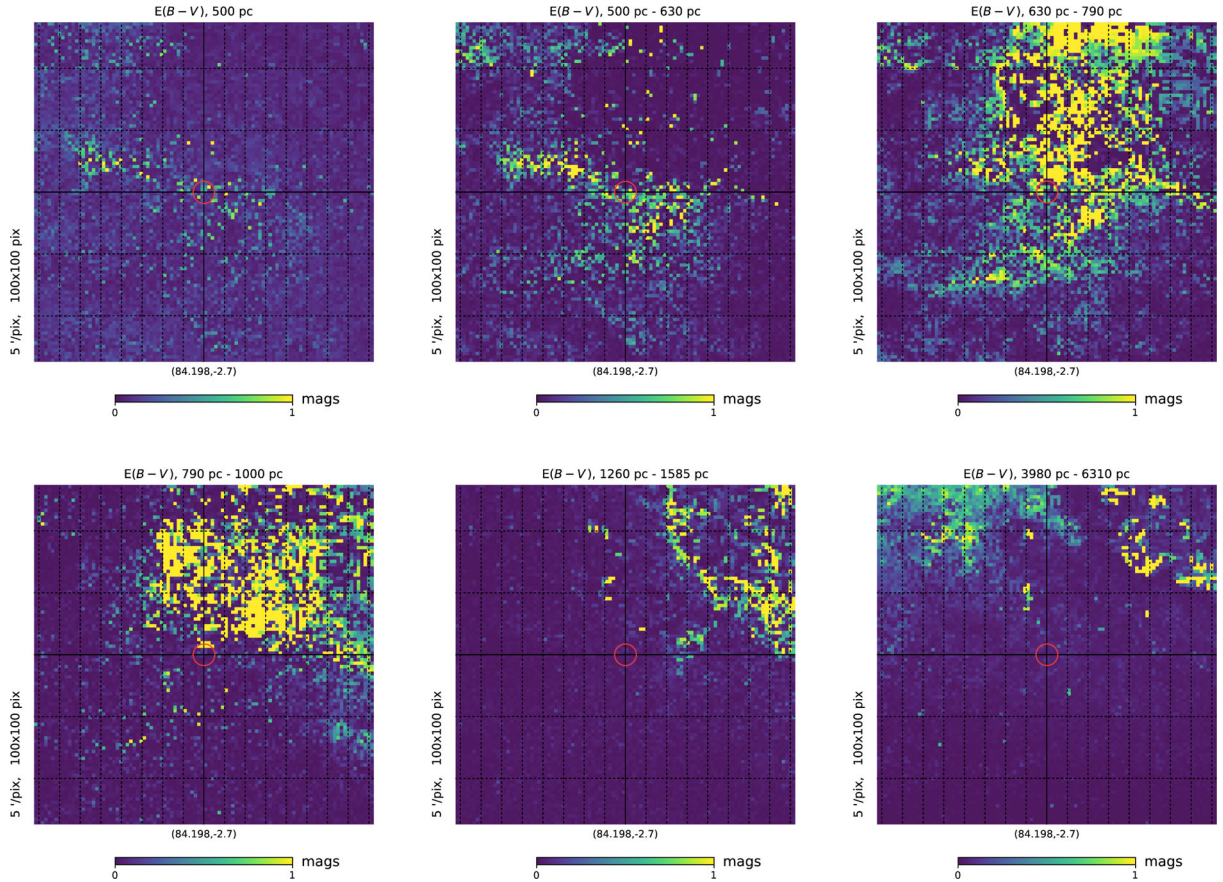


**Figure 10.** Pan-STARRS 1 extinction maps along the line of sight of GRB 160623A (Galactic coordinates  $l = 84.2$ ,  $b = -2.7$ ). Each pixel in the map is 5 arcmin, for a total of  $100 \times 100$  pixels, and the red circle represents the *XMM-Newton* field of view. The maps are evaluated at the distances found for the rings: the largest extinction is placed in the range 630–790 pc, i.e. at the position of ring 3, which is also the one with the highest column density.



Finally, the Pan-STARSS 1 survey provides a three-dimensional picture of the interstellar reddening ( $E(B - V)$ ), over 3/4 of the sky out to a distance of several kpc (Green et al. 2015). We investigated the extinction in a region of 500 arcmin  $\times$  500 arcmin around the direction of GRB 160623A, by examining the maps for various ranges of distances centred at the values derived for the dust layers (see Fig. 10). The maps show that the distribution of the Galactic medium in this direction is complex, with filaments and asymmetries. High levels of extinction are seen at distances of 500, 500–630, 630–790 and 790–1000 pc, while at larger distances the extinction is weaker. In particular, we note that the largest extinction is in the range 630–790 pc, i.e. around the distance of the dust layer of ring 3, which is the one with the highest column density. This demonstrates that the two approaches provide similar results, further corroborating the analysis presented here. However, we highlight that our approach in this specific case can be more powerful. In fact, the Pan-STARSS 1 extinction map is strongly dependent on the existence of known stars at the different distances. Instead we just need to know the expansion law of the dust-scattering rings, allowing us to map the Galaxy with an extremely high resolution. Finally, we note that in this work we assumed isotropy for the dust layers. This does not change the derived distances but affects the values of the column densities of the dust layers. Although beyond the scope of this paper, we found possible hints of azimuthal asymmetry in the rings, due to more dust in particular towards the direction of the Galactic plane (right-hand side in Fig. 1). This would be, again, consistent with the extinction maps of the Pan-STARSS 1 survey. However, we note that the constraints on the azimuthal asymmetry are very weak and no robust claim can be made.

## ACKNOWLEDGEMENTS

This work has been partially supported through financial contribution from PRIN INAF 2014. The results are based on observations obtained with *XMM-Newton*, an ESA science mission with instruments and contributions directly funded by ESA Member States and NASA, and on data obtained from the HEASARC archive. PE acknowledges funding in the framework of the NWO Vidi award A.2320.0076. EC acknowledges support from a VIDI grant from the Netherlands Organisation for Scientific Research (NWO). We thank Daniele Viganò who developed part of the software used in this work.

## REFERENCES

Arnaud K. A., 1996, in Jacoby G. H., Barnes J., eds, ASP Conf. Ser. Vol. 101, *Astronomical Data Analysis Software and Systems V*. Astron. Soc. Pac., San Francisco, San Francisco, p. 17  
 Beardmore A. P., Willingale R., Kuulkers E., Altamirano D., Motta S. E., Osborne J. P., Page K. L., Sivakoff G. R., 2016, *MNRAS*, 462, 1847

Castro-Tirado A. J. et al., 2016, *GCN*, 19710, 1  
 Costantini E., Freyberg M. J., Predehl P., 2005, *A&A*, 444, 187  
 Dame T. M., Hartmann D., Thaddeus P., 2001, *ApJ*, 547, 792  
 Dickey J. M., Lockman F. J., 1990, *ARA&A*, 28, 215  
 Draine B. T., 2003, *ApJ*, 598, 1026  
 Evans P. A. et al., 2009, *MNRAS*, 397, 1177  
 Evans P. A. et al., 2014, *MNRAS*, 444, 250  
 Frederiks D. et al., 2016, *GRB Circ.*, 19554, 1  
 Green G. M. et al., 2015, *ApJ*, 810, 25  
 Hasenberger B., Forbrich J., Alves J., Wolk S. J., Meingast S., Getman K. V., Pillitteri I., 2016, *A&A*, 593, A7  
 Heinz S. et al., 2015, *ApJ*, 806, 265  
 Heinz S., Corrales L., Smith R., Brandt W. N., Jonker P. G., Plotkin R. M., Neilsen J., 2016, *ApJ*, 825, 15  
 Jin C., Ponti G., Haberl F., Smith R., 2017, *MNRAS*, 468, 2532  
 Kalberla P. M. W., Burton W. B., Hartmann D., Arnal E. M., Bajaja E., Morras R., Pöppel W. G. L., 2005, *A&A*, 440, 775  
 Malesani D. et al., 2016, *GRB Circ.*, 19708, 1  
 Mathis J. S., Lee C.-W., 1991, *ApJ*, 376, 490  
 Mathis J. S., Rumpl W., Nordsieck K. H., 1977, *ApJ*, 217, 425  
 Mingo B. et al., 2016, *GRB Circ.*, 19558, 1  
 Miralda-Escudé J., 1999, *ApJ*, 512, 21  
 Pintore F., Mereghetti S., Tiengo A., Vianello G., Costantini E., Esposito P., 2017, *MNRAS*, 467, 3467  
 Predehl P., Burwitz V., Paerels F., Trümper J., 2000, *A&A*, 357, L25  
 Read A. M., Rosen S. R., Saxton R. D., Ramirez J., 2011, *A&A*, 534, A34  
 Rice T. S., Goodman A. A., Bergin E. A., Beaumont C., Dame T. M., 2016, *ApJ*, 822, 52  
 Shao L., Dai Z. G., 2007, *ApJ*, 660, 1319  
 Smith R. K., Dwek E., 1998, *ApJ*, 503, 831  
 Strüder L. et al., 2001, *A&A*, 365, L18  
 Svirski G., Nakar E., Ofek E. O., 2011, *MNRAS*, 415, 2485  
 Tiengo A., Mereghetti S., 2006, *A&A*, 449, 203  
 Tiengo A. et al., 2010, *ApJ*, 710, 227  
 Tiengo A., Vianello G., Esposito P., Salvaterra R., 2016, *GRB Circ.*, 19559, 1  
 Trümper J., Schönfelder V., 1973, *A&A*, 25, 445  
 Turner M. J. L. et al., 2001, *A&A*, 365, L27  
 Vasilopoulos G., Petropoulou M., 2016, *MNRAS*, 455, 4426  
 Vaughan S. et al., 2004, *ApJ*, 603, L5  
 Vianello G., Tiengo A., Mereghetti S., 2007, *A&A*, 473, 423  
 Vianello G., Dirirsa F., Omodei N., Racusin J. L., Axelsson M., Kocevski D., 2016, *GRB Circ.*, 19553, 1  
 Vuong M. H., Montmerle T., Grosso N., Feigelson E. D., Verstraete L., Ozawa H., 2003, *A&A*, 408, 581  
 Wang Y.-Z., Zhao Y., Shao L., Liang E.-W., Lu Z.-J., 2016, *ApJ*, 818, 167  
 Willingale R., Starling R. L. C., Beardmore A. P., Tanvir N. R., O’Brien P. T., 2013, *MNRAS*, 431, 394  
 Wilms J., Allen A., McCray R., 2000, *ApJ*, 542, 914  
 Zhao Y.-N., Shao L., 2014, *ApJ*, 789, 74  
 Zubko V., Dwek E., Arendt R. G., 2004, *ApJS*, 152, 211

This paper has been typeset from a  $\text{\LaTeX}$  file prepared by the author.